Compartmental approach for modelling twin-screw granulation using population balances

Hamza Y. Ismail[1,2], Saeed Shirazian[2], Mehakpreet Singh[1,2,*], Darren Whitaker[1], Ahmad B. Albadarin[1,2], Gavin M. Walker[1,2]

[1] Pharmaceutical Manufacturing Technology Centre, Bernal Institute, University of Limerick, Limerick, Ireland

[2] Department of Chemical Sciences, Bernal Institute, University of Limerick, Limerick, Ireland

[*] Corresponding author: Mehakpreet.Singh@ul.ie

Tel.: +353 (08) 99816927

Abstract

In this study, a compartmental population balance model (CPBM) is developed as a predictive tool of particle size distribution (PSD) for wet granulation in co-rotating twin-screw granulator (TSG). This model is derived in terms of liquid to solid ratio (L/S) and screw speed representing the main process parameters of the TSG. The mathematical model accounts for aggregation and breakage of the particles occurring in five compartments of the TSG with inhomogeneous screw configurations (3 conveying zones and 2 kneading zones). Kapur's aggregation kernel is implemented in granulation and finite volume numerical method is adapted for solving the mathematical model. The results show a dramatic improvement in solution accuracy compared to the cell average numerical method. Moreover, Kriging interpolation is used to interpolate for new values of empirical parameters at different L/S and screw speeds. Finally, the CPBM model is calibrated and validated using the experimental data.

Keywords: Compartmental population balance models; Finite Volume Numerical Method; Kapur kernel; Twin-screw granulation; Kriging interpolation.

1. Introduction

Pharmaceutical industry is trying to shift from batch to continuous manufacturing due to the advantages that continuous drug manufacturing brings with ease in scale up, reduction of production time, more flexibility in powder production and, most importantly, better quality control. In order to develop a continuous manufacturing with better quality by design control, the continuous units should be designed and accurately inter-connected to ensure optimum drug quality without the need for corrective processes. This can only be achieved with an accurate understanding and modelling of the continuous manufacturing processes [1], [2],[3], [4].

Twin-screw granulation is a continuous granulation process that provides superior efficiency in granulating powders with short residence time, efficient use of binder, better control of granule properties, and effective mixing of active pharmaceutical ingredients (APIs) and excipients [5], [6]. Because of these properties, TSG is gaining more popularity in continuous granulation of pharmaceutical powders. In order to operate the twin-screw granulator effectively on quality by design (QbD) production standards, a model should be derived for the continuous granulation in twin-screw based on the mechanistic understanding of the processes occurring. In this way, the model can quantitatively describe the effect of the process, material or design parameters on the critical quality attributes of the granules produced. This type of mechanistic modelling is crucial to facilitate the QbD approach that states ‘‘*quality cannot be tested into products; it should be built-in or should be by design*’’[7] and is needed for continuous granulation of pharmaceutical powder in a co-rotating twin screw.

Mechanistic models that describe wet granulation are either on microscale like discrete elemental modelling (DEM) or macro-scale like population balance modelling (PBM). DEM is based on solving Newton’s laws of motion and kinetic interactions for each individual particle, and keeping track of the particles external and internal properties including velocity,

acceleration, spatial coordinates and size. DEM is computationally very expensive since it solves all of these equations for each particle at each time interval, thus it is usually applied on a small portion of the system or when the particles under investigation are few [8]. PBM is used to study a large population of particles by tracking the change in their properties such as size, shape and velocity over time by accounting for the mechanisms occurring in the process such as nucleation, growth, aggregation and breakage [9], [10],[11], [12],[13], [14] . Recently some hybrid models have been created by combining DEM and PBM to utilise the advantages of both modelling approaches [15], [16].

PBM is a powerful tool that is very popular in modelling particulate processes including granulation. PBM is commonly used for modelling wet granulation where nucleation, growth aggregation, attrition and breakage of particles can occur simultaneously [9]. PBM for wet granulation is used in batch and continuous operating units [17]–[20] including co-rotating twin screw and the most important factors are the kinetics of the mechanisms considered and which represents the rate at which these mechanisms occur based on statistical probability or empirical equations. Aggregation and breakage are usually considered as the dominant mechanisms in TSG as reported by Lui et al. [21]. PBM is an integro-partial differential equation that requires discretization using numerical methods in order to obtain the solution, thus many numerical techniques were developed to solve this equation including Hounslow discretization [22], fixed pivot method [23], and cell average (CA) [24] with the latter being effective in minimizing mass loss in the system. The sectional method such as cell average technique has a very complex mathematical formulation and large number of bins are required to predict the mass conservation property accurately due to the distribution of the particles to the neighbouring nodes. In order to overcome this issue, recently developed finite volume scheme used by Saha et al., Tsotsas et al. and Singh et al. [25], [26], [27] is mathematically simple and easy to adapt for solving the granulation model. In this work, the finite volume

numerical method (FVNM) is used for the first time to solve a 1-D CPBM of wet granulation in TSG.

Aggregation and breakage processes are the dominant mechanisms in twin-screw wet granulation. In order to model the aggregation kinetics, earlier studies [17], [21] used the sum kernel in granulation of pharmaceutical powders due to its simplicity. However, it does not provide enough flexibility in controlling the aggregation rate. Whereas, due to the additional denominator term, Kapur's kernel provides a mathematical flexibility for controlling the kinetics [28]. Therefore, in this article Kapur's kernel is used as the aggregation rate for the first time in the CPBM of TSG.

Aggregation and breakage kernels depend on empirical parameters that are calculated by fitting the predicted PSD of the PBM and the experimental PSD obtained from experiments [17], [21]. These empirical parameters change for each run corresponding to the experimental conditions (material, process or design parameters) as reported by Lui et al. [21]. In his work Lui et al. [21] used the sum and binary breakage kernel while Van Hauwermeiren et al.[17] used a lumped hypergeometric for describing the aggregation frequency in combination with breakage (combination of binary breakage and attrition). In this work, Kapur kernel is tested against sum kernel for aggregation mechanism and a binary breakage is considered. The empirical parameters in the kernels were fitted for polynomial equations form in terms of screw configuration, screw speed and throughput. Moreover, Dhenge et al. and Meng et al. [29], [30] have experimentally shown that liquid to solid ratio (L/S) is the main process parameters that affect the PSD in twin-screw granulation. Therefore, in this article, a CPBM will be derived to predict the PSD in terms of L/S ratio, screw speed and spatial inhomogeneity of the screw configurations (conveying and kneading elements).

2. Population balance model (PBM) & Modelling methodology

In this work PBM is used for modelling the particle size distribution of the granules produced from the twin-screw granulator. The PBM for tracking the change of the granule size number distribution due to aggregation and breakage at steady state is expressed as follows:

$$\frac{dn(u,t)}{dt} = B(u,t) - D(u,t). \quad (1)$$

Here, *n* represents the number density function of particles of volume *u* at time *t*. Since, aggregation and breakage are the dominant mechanisms in twin-screw granulation [21], [5], [31] therefore, the *B* and *D* terms in equation (1) refer to birth and death rates of particles due to aggregation and breakage mechanisms. Birth due to aggregation can be expressed by Ramkrishna [32] as follows:

$$B_{agg}(t,u) = 1/2 \int_0^u \beta(t,u-\epsilon,\epsilon) n(t,u-\epsilon) n(t,\epsilon)\, d\epsilon, \quad (2)$$

which gives the birth rate of particle of size u due to aggregation of particles of sizes $u-\epsilon$ and ϵ respectively. Moreover, $\beta(t,u,\epsilon)$ is the aggregation kernel which is symmetric in nature.

Similarly, death rate due to aggregation mechanism can be expressed as:

$$D_{agg}(t,u) = n(t,u) \int_0^\infty \beta(t,u,\epsilon) n(t,\epsilon)\, d\epsilon \quad (3)$$

where $D_{agg}(t,u)$ denotes death rate of particle of size u at time t due to the aggregation with particle ϵ.

In addition, the birth and death rates due to breakage mechanism given by Ramakrishna [32] can be written as:

$$B_{br}(t,u) = \int_u^\infty b(u,\epsilon) S(\epsilon) n(t,\epsilon)\, d\epsilon, \quad (4)$$

$$D_{br}(t,u) = S(u) n(t,u). \quad (5)$$

Here $b(u,\epsilon)$ is the probability density function of the formation of particles of size u from breakage of particles of size ϵ and $S(\epsilon)$ is the selection function.

Therefore, the birth and death rates in equation (1) are written as:

$$B(u,t) = B_{agg}(t,u) + B_{br}(t,u), \tag{6}$$

$$D(u,t) = D_{agg}(t,u) + D_{br}(t,u). \tag{7}$$

Thus equation (1) can be rewritten as follows:

$$\frac{dn(u,t)}{dt} = \frac{1}{2}\int_0^v \beta(t,u-\epsilon,\epsilon)n(t,u-\epsilon)n(t,\epsilon)\,d\epsilon -$$

$$n(t,u)\int_0^\infty \beta(t,u,\epsilon)n(t,\epsilon)\,d\epsilon + \int_u^\infty b(u,\epsilon)S(\epsilon)n(t,\epsilon)\,d\epsilon - S(u)n(t,u). \tag{8}$$

The most important terms in above equation are the aggregation and breakage kernels β and S that represent the rate of aggregation and breakage of the particles, respectively. For this work, Kapur and sum aggregation kernels are implemented and compared whose mathematical structures are provided in equations (9) and (10), respectively.

$$\beta = \frac{\beta_0(u_i+u_j)^a}{(u_i u_j)^b}, \tag{9}$$

$$\beta = \beta_0(u_i+u_j)^a, \tag{10}$$

where, u_i and u_j are the volumes of two aggregating particles. β_0, a and b are empirical parameters need to be calibrated for certain experimental conditions. In this work, β_0, a and b will be represented in terms of the twin screw process parameters (L/S ratio and screw speed).

For the breakage kernel, the commonly used power law function is considered:

$$S(v) = S_0 u^k \tag{11}$$

where S_0 is the selection constant and k is a power exponent, and they will be calibrated according to the experimental conditions. Moreover, S_0 and k will also be represented in terms of L/S and screw speed.

Binary breakage distribution of the following form will be implemented as given below:

$$b(u, \epsilon) = 2/\epsilon, \tag{12}$$

where ϵ is volume of the mother particle that is broken equally into two particles with size u.

The model assumes a spherical morphology of the powder. All the empirical parameters (β_0, a, b, S_0 and k) in both aggregation and breakage kernels will be represented in terms of the process parameters.

In this work, two screw configurations (conveying and kneading) are used in twin screw granulation. These configurations consist of 3 conveying (CZ) and 2 kneading zones (KZ) (as shown in Figure 1), each screw configuration is described by a rate of aggregation and breakage. In this study two types of screw configurations are considered and can be differentiated based on the rates in each zones as they depend on empirical parameters in the aggregation and breakage kernels. To account for this spatial inhomogeneity in the system, the PBM model will be applied on the 5 zones of the twin screw and the granules at the end of each zone are considered as the input for the following zone. It is also assumed that the liquid is uniformly distributed over the particles in all zones, and no mixing of material between the zones occur.

In other words, the CPBM accounts for aggregation and breakage in each compartment assuming that the aggregation and breakage empirical parameters is dependent on the screw

configuration (conveying screw configuration has different parameters than the kneading screw configuration).

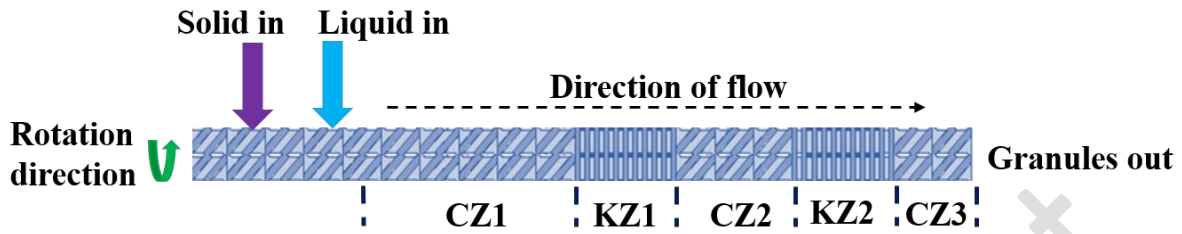

Figure 1: Schematic representation of compartmental model for TSG.

For building a predictive CPBM in terms of L/S and screw speed, first nine experimental runs are conducted at various L/S and screw speed, and the PSD is measured for each run. Then, the values of the empirical parameters (β_0(CZ), a(CZ), b(CZ), S_0(CZ), K(CZ), β_0(KZ), a(KZ), b(KZ), S_0(KZ) and K(KZ)) are determined by fitting the experimental and predicted PSD for eight runs. This is done by minimizing the SSE between the experimental and predicted PSDs using Genetic Algorithm (GA) in Matlab.

Second, the kriging interpolation is used to increase the number of data points for the empirical parameters at new process parameter points, and then the empirical parameters are fit in terms of the process parameters using polynomial structures.

Finally, the predicted PSD from the CPBM is validated against the experimental PSD. The full schematic representation of the modelling methodology is depicted in Figure 2.

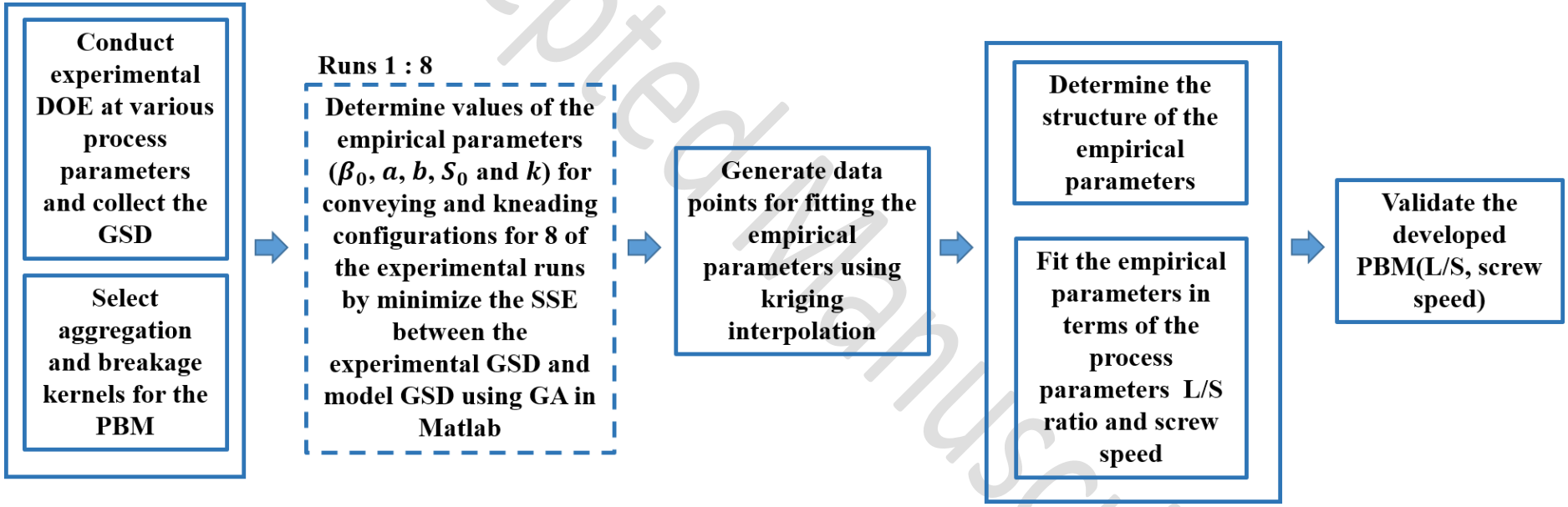

Figure 2: Scheme diagram of the modelling methodology used in building the PBM in terms of L/S ratio and screw speed

3. Experimental procedure

Microcrystalline cellulose (MCC-101, Avicel PH 101, obtained from Pharmatrans, Switzerland) was granulated with water in a twin-screw extruder, ZE12 (ThreeTec, Switzerland) having screw diameter 12 mm and length-to-diameter ratio 40:1. The screws were configured with two kneading blocks angled at 60° facing forward (refer to Figure 3), with 6 and 5 kneading elements in the first and second blocks, respectively. A syringe pump was used for feeding water as binder and a gravimetric feeder (Three-Tec, Switzerland) for feeding the powder. The experimental setup is shown below in Figure 4.

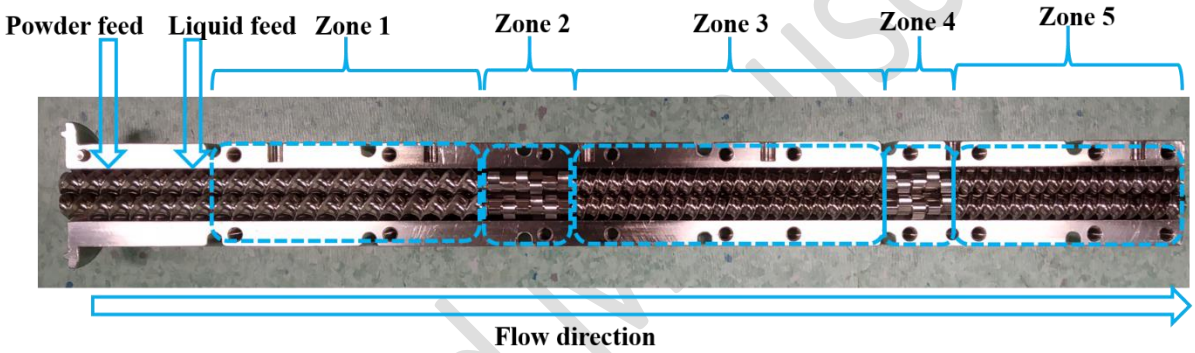

Figure 3: Screw configuration used in the wet granulation experiments.

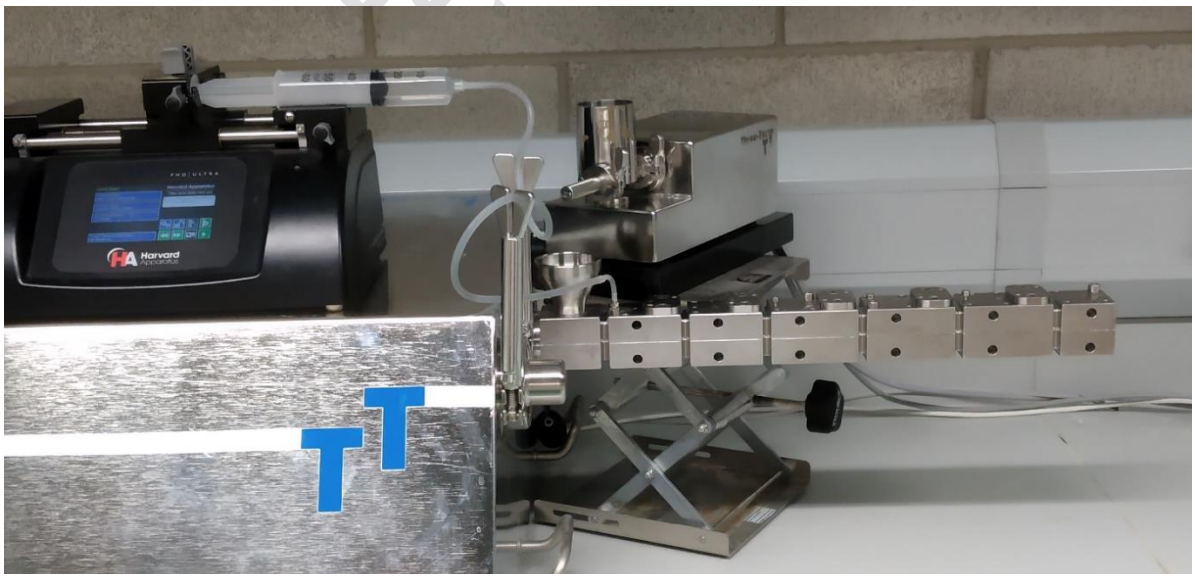

Figure 4: Twin-screw granulator experimental setup used for the experimental runs.

The liquid to solid ratio (*L/S*) was varied from 0.9 to 1.3 by adjusting liquid feed rates, while keeping the powder feed rate constant at 100 g/h, and the screw speed was also varied from 50 to 200 rpm (see Table 1). The obtained granules were collected at the outlet of the twin screw for analysis after the extruder reached steady state, which was determined by monitoring the torque measured by the apparatus [33].

Table 1: DOE of the Experimental runs done at various L/S ratio and screw speed.

Runs	Liquid feed rate (g/h)	Powder feed rate (g/h)	L/S ratio	Screw speed (rpm)
1	90	100	0.9	50
2	90	100	0.9	100
3	90	100	0.9	200
4	110	100	1.1	50
5	110	100	1.1	100
6	110	100	1.1	200
7	130	100	1.3	50
8	130	100	1.3	100
9	130	100	1.3	200

In additional to the nine runs conducted in the DOE (Table 1) two runs (run 10 and 11) are also conducted with random L/S and screw speeds chosen to be 1.05, 1.15 and 170 and 150 rpm respectively at the same powder flow rate of 100 g/hr. Runs 10 and 11 are later used in addition to one run from the DOE for validating the developed CPBM.

The resultant mixtures of fines and granules were dried for 15 hours in an oven at 40 $^{\circ}$C and then characterized using dry powder dispersion laser diffraction (Microtrac S3500), the granules were first sieved and all the particles were less than 1400 microns before entering the Microtrac.

The mean residence time of particles inside the barrel of the granulator was determined from an empirical artificial neuron network (ANN) equation derived and validated experimentally

based on previous work [34]. The derived model for the mean residence time of particles is linearly dependent on the L/S ratio and screw speed as given below:

$$\lambda = 162.2 + 55.1\frac{\mathrm{L}}{\mathrm{S}} - 0.1179\mathrm{SS} - 0.0822\phi, \tag{13}$$

where λ is the predicted mean residence time (s), L/S is the liquid to solid ratio, SS is the screw speed (rpm), and ϕ is the powder flow rate (g/h). The mean residence time in the twin screw which is used as limits to integrate the time domain in equation 8.

4. Numerical approximation

In this article, the finite volume numerical method (FVNM) as developed by developed finite volume scheme used by Saha et al., Tsotsas et al. and Singh et al. [25], [26], [27] is adapted for solving the CPBM in TSG. Also, the existed cell average numerical method (CANM) was implemented and compared with FVNM for demonstrating the advantage of FVNM over CANM. For detailed explanation of CANM (refer to Appendix A).

For discretizing the internal coordinate, a finite one-dimensional computational domain with upper limit $u_{max} < \infty$ is taken and divided into *I* number of smaller cells having u_i as representative volume, for $i = 1, 2, 3, \ldots, I$ (as shown in Figure 5). Indeed, the representative volume in each cell equals the arithmetic average of two cell boundaries. The main idea of the FVNM is to convert the continuous eq. (8) into a set of *I* ordinary differential equations (ODEs).

$$u_{\frac{1}{2}} = 0,\ u_i = (u_{i+\frac{1}{2}} + u_{i-\frac{1}{2}})/2,\ \Delta u_i = u_{i+\frac{1}{2}} - u_{i-\frac{1}{2}}.$$

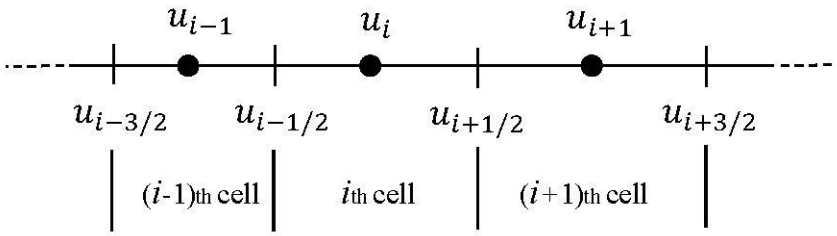

Figure 5: One dimensional domain discretization.

We denote the number of particles in the *i*th cell by N_i,

$$N_i = \int_{u_{i-\frac{1}{2}}}^{u_{i+\frac{1}{2}}} n(t,u)du. \tag{14}$$

The distribution is then represented by a series of delta functions,

$$n(t,u) = \sum_{i=1}^{I} N_i\, \delta(u-u_i). \tag{15}$$

Substituting this form into equation (8) we obtain a set of ODE's given by

$$\frac{dN_i}{dt} = B_i - D_i. \tag{16}$$

In the FVNM, the birth and death terms for *i*th cell in equation (16) corresponding to simultaneous aggregation and breakage mechanisms are given as follows:

$$\frac{dN_i}{dt} = \sum_{(j,k)\in\gamma^i} \beta\left(u_j,u_k\right) N_j N_k \frac{\Delta u_j \Delta u_k}{\Delta u_i}\omega_{j,k}^b - \sum_{j=1}^{I} \beta\left(u_i,u_j\right) N_i N_j \Delta u_j\, \omega_{j,k}^d +$$

$$\sum_{k=i}^{I} S_k N_k\, \theta_k^b \int_{u-\frac{1}{2}}^{p_k^i} b(u,u_k)du - S_i\, N_i\, \theta_k^d\,. \tag{17}$$

The first summation on the right-hand side is taken over all pairs (j,k) such that the sum of midpoints $u_j + u_k$ falls in interval i. This condition may be expressed formally as:

$$\gamma^i = \left\{(j,k)\; N\times N : u_{i-\frac{1}{2}} \le \left(u_j+u_k\right) < u_{i+\frac{1}{2}}\right\}. \tag{18}$$

The factor $\omega_{j,k}^b, \omega_{j,k}^d, \theta_k^b$ and θ_k^d are the weights responsible for the conservation of total mass in the system and preservation of the total number in the system which are given below:

$$\omega_{j,k}^b = \frac{u_j+u_k}{2u_{l_{jk}}-(u_j+u_k)} \quad , \qquad \omega_{j,k}^d = \frac{u_{j_{jk}}}{2u_{l_{jk}}-(u_j+u_k)}. \tag{19-20}$$

and

$$\theta_k^b = \frac{u_k[v(u_k)-1]}{\sum_k^{i-1}(u_k-u_i)\int_{u-\frac{1}{2}}^{p_k^i} b(u,u_k)du} \quad , \quad \theta_k^d = \frac{\theta_k^b}{u_i}\sum_k^{i-1} u_k \int_{u-\frac{1}{2}}^{p_k^i} b(u,u_k)du \qquad (21\text{-}22)$$

$$\text{where } p_k^i = \begin{cases} u_k, i = k \\ u_{k+1/2}, \text{ otherwise.} \end{cases}$$

The detailed formulation of the finite volume scheme can be found in Saha et al., Tsotsas et al. and Singh et al. [25], [26], [27]. It is very important to notice that for the cell average technique, there is always the possibility of numerical diffusion when the particles properties are distributed to the neighbouring nodes after averaging of the particles properties, as reported by Kumar et al. 2009 [35]. However, for the finite volume scheme, no such distribution is required as only correction factors are added to the formulation to ensure the mass conservation and number preservation property. Hence, the possibility of losing mass from the system is less in FVNM than the CANM.

A 20 nonlinear grid was used for discretizing the given domain in the following way:

$$I\,(i) = I\,(i-1)\ \times \log(i)\ \ for\ i > 2 \qquad (23)$$

where I represents the boundary of each cell, and i is the cell number. The particle volume in the first bin boundary, that is, I (1) and I (2) were assumed 1 x 10^{-17} m^3 and 4 x 10^{-16} m^3 respectively and 20 size bins were used.

5. Parameter estimation and Kriging interpolation

The empirical parameters in the aggregation and breakage kernels are determined by minimizing the sum of squared error (SSE) between the experimental and predicted PSD as in equation (24). Eight out of nine experimental runs are used to determine the values of the empirical parameters and one run is used for validating the final CPBM developed after

replacing the empirical parameters by their equations in terms of the process parameters (L/S and screw speed).

Different coefficients are used for different screw configurations (CZ and KZ). The full CPBM comprised of eight empirical parameters when a sum kernel is used and ten empirical parameters when a Kapur kernel is considered. Least square method of optimisation is used given as follows:

$$OF_j\ (X) = \sum_{i=1}^{P}(n_i(X) - y_i)^2, \tag{24}$$

where *OF* is the objective function SSE at run *j* which is a function of empirical parameters *X*, $n_i(X)$ is the predicted volume density in *i*th bin calculated from the PBM at value of X. Additionally, y_i is the measured density at size bin i from experimental run j, and p is the number of discretized bins used for the granule size distribution. It is important to note that the values in the objective function are the volume percentage varying between 0 to 100 rather than between 0 to 1 to prevent impairing the optimisation. Moreover, to observe the ability of the model in predicting of the shape of PSD, the experimental data are fitted in the PSD rather than fitting on the *d*-values of PSD.

Genetic algorithm method is used to minimise the objective function which can be defined as squares of difference between observed and simulated data points. The optimisation is conducted using MATLAB 2015b, *Mathworks* software via *Genetic Algorithm* (GA) optimisation tool. Given that GA is not dependent on an initial guess, the global minimum is obtained for the objective function. Sum of squared errors (SSE) and the coefficient of determination (R^2) were used to indicate the accuracy of the fitting.

Ordinary kriging interpolation is used to increase the number of data points for fitting by interpolating values of the empirical parameters at new process parameter (L/S and screw

speed) points. Nelder-Mead simplex direct search optimization is used for obtaining the variogram for ordinary kriging interpolation.

Ten two-dimensional kriging interpolations are conducted on the empirical parameters calibrated from eight experimental runs obtained from twin screw granulation at various L/S and screw speed (Table 1) to predict the empirical parameters at new process parameters (L/S and screw speed). The mathematical description of the ordinary Kriging interpolation is provided in Appendix F.

Kriging is performed in *Matlab* 2015b, *Mathworks* where L/S ratio and screw speed are used as input parameters and the empirical parameters as output parameters. Interpolation is conducted at five new points for each dimension in which 36 points were obtained after applying kriging in a 2-D numerically meshed system. The interpolated kriging data are used to fit the empirical parameters in terms of L/S and screw speed (rpm) in a polynomial form. Interpolated data are provided in the supplement excel sheet in Appendix B.

7. Results and discussion

7.1. Experimental results

The experimental results collected for the PSD for each run are presented in Figures 6 (b), (c) and (d) for L/S ratio 0.9, 1.1, and 1.3 respectively and for each screw speed of 50, 100, and 200 rpm represented with the dotted, dashed and solid lines, respectively. Figure 6 (a) also shows the initial particle size distribution of MCC-101 before granulation; this is used as the initial particle size distribution (PSD) in the CPBM.

(a)	(b)
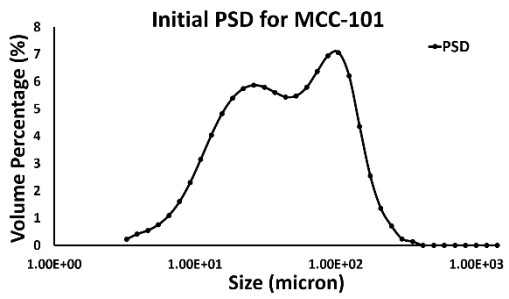	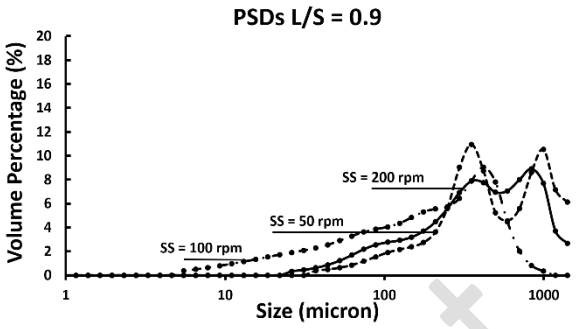
Initial PSD of MCC-101	PSDs for runs 1, 2, and 3 with L/S ratio of 0.9
(c)	**(d)**
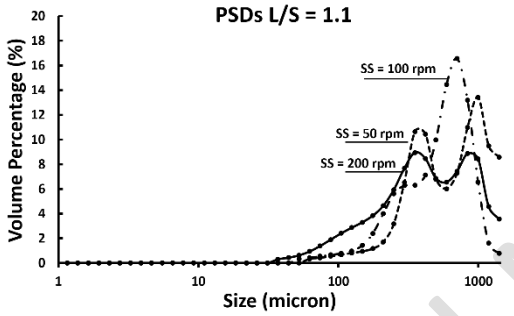	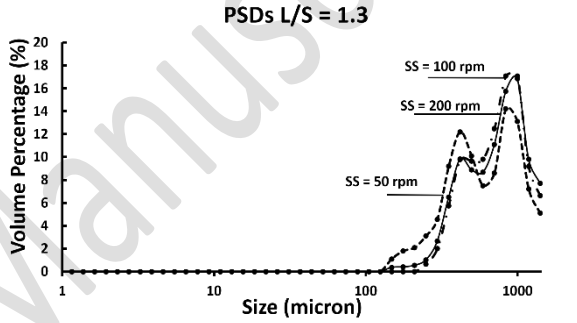
PSDs for runs 4, 5 and 6 with L/S ratio1.1	PSDs for runs 7, 8 and 9 with L/S ratio of 1.3

Figures 6: PSDs of MCC-101 before granulation and after granulation at various L/S ratios and screw speeds 50, 100, and 200.

The results show that increasing the L/S ratio increases the granule size significantly where the particle size distribution is shifted more to larger size bins as the L/S ratio moves from 0.9 to 1.1 and 1.3, as can be seen in Figures 6 (b), (c), and (d), respectively. On the other hand, screw speed does not show a monotonic effect on granule size throughout the whole L/S ratio range, where at low and medium L/S ratio (0.9 and 1.1) the lowest screw speed produces the biggest granules while at higher L/S ratio (1.3) the screw speed seems to have less effect on determining the granule size (Figure 6 (d)). The L/S ratio is the dominant parameter in determining the granule size and this is mainly due to the aggregation mechanism which depends on the liquid content of the particle. More aggregations occur between particles having

more liquid content, and with the aggregation being dominant the breakage is masked out and the granules grows faster.

Two random runs at L/S ratio and screw speed of 1.05, 1.15 and 170 and 150 rpm respectively where conducted and used later for validating the CPBM. The experimental PSDs obtained for these two runs are given in the figures a and b of Table 2.

Table 2: Experimental PSDs for the two additional runs used for model validation.

(a)	**(b)**
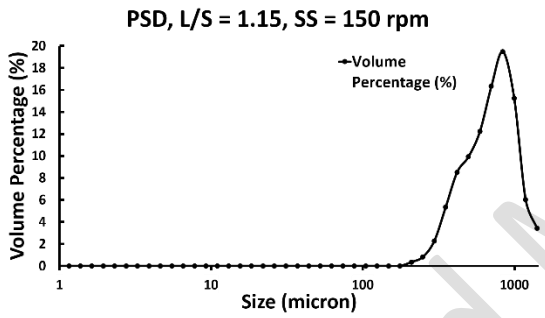	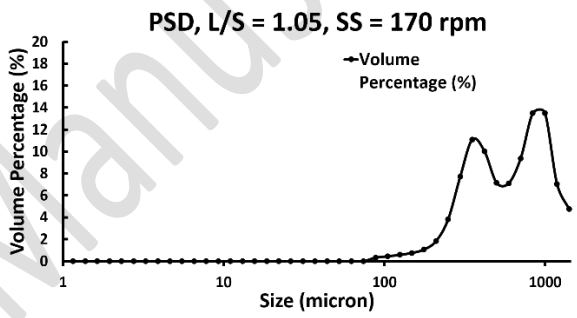
Run 10 : PSD at L/S ratio of 1.15 and SS 150 rpm	Run 11 : PSD at L/S ratio of 1.05 and SS = 170 rpm

Eight of the nine experimental data of particle size distributions shown in Figures 6 (a), (b), (c), and (d) are used in calibrating the empirical parameters in the aggregation and breakage kernels and one is used for validation in additional to runs 10 and 11.

7.2. Effect of Aggregation Kernel

Choosing the right kernels is very important in calibrating the empirical parameters. A Kapur kernel is implemented and compared with a sum kernel to determine the best fit of the experimental and predicted PSDs and thus obtain the best calibration of the empirical

parameters. The importance of the Kapur's kernel over the sum kernel is provided in section 1.

The developed PBM is calibrated using the experimental data collected by minimizing the SSEs between the experimental PSD collected and the PSD predicted by the PBM for eight runs by calibrating the empirical parameters in the aggregation and breakage kernels. Kapur and sum kernels are incorporated in the CPBM, where Kapur kernel has three empirical parameters (β_0, a and b) and sum kernel has two empirical parameters (β_0 and a) and the breakage kernel has two empirical parameters (S_0 and k). Thus, when using the Kapur kernel an overall of ten empirical parameters should be calibrated in the CPBM for two screw configurations. However, for the sum kernel, eight empirical parameters are calibrated. FVNM is implemented in solving the CPBM equations as explained in section 5.

The SSEs are minimized using Genetic Algorithm in Matlab, and the values of the empirical parameters after optimization are given in Appendix C. The experimental PSDs and predicted PSDs from the calibrated CPBM for eight runs are presented graphically in Figures 7 and 8 for Kapur and sum kernels, respectively.

Table 3: SSE between the experimental and predicted PSDs after calibration using FVNM.

Runs	Kapur kernel	Sum kernel
1	0.00979	0.029312
2	0.004154	0.004261
3	0.00821	0.00281
4	0.006215	0.0108
5	0.002098	0.002634
6	0.001605	0.001653
7	0.005147	0.0063
9	0.003525	0.00623

Kapur's kernel shows a more accurate prediction of the PSDs compared to the sum kernel as the average SSE obtained using the sum kernel's is 1.58 times higher than Kapur's kernel (Table 3). This is due to the fact that Kapur's kernel has a denominator term, dependent on the multiplication of the particles' volumes and an empirical power constant (*b*) that gives more flexibility in controlling the aggregation rate even when particles grow bigger. However, for sum kernel no such denominator term is present which controls aggregation. This flexibility in Kapur's kernel conquer certain rates that the sum kernel cannot reach which gives a better estimation of the empirical parameter.

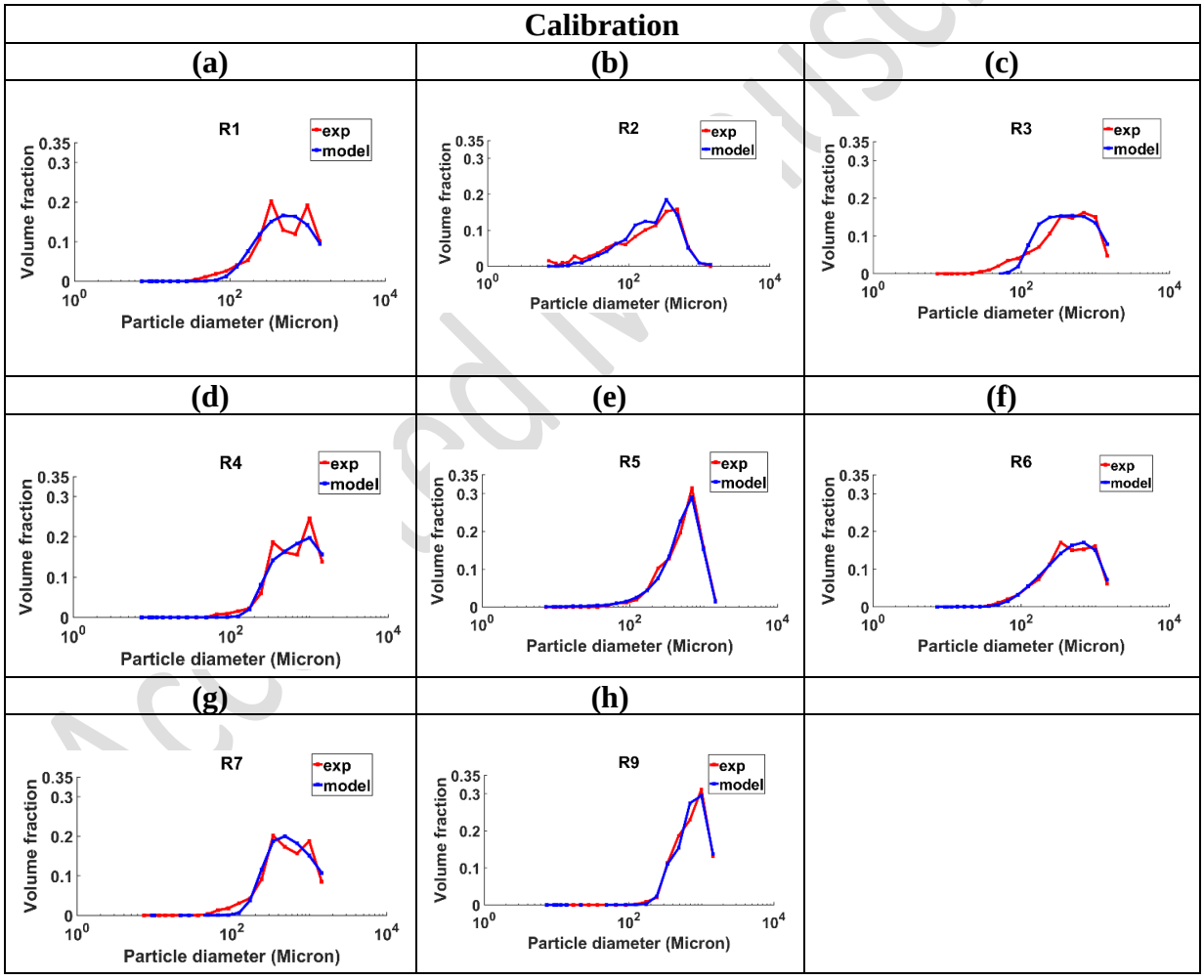

Figure 7: Experimental vs. predicted PSDs for calibrating the empirical parameters using Kapur kernel with FVNM.

Calibration

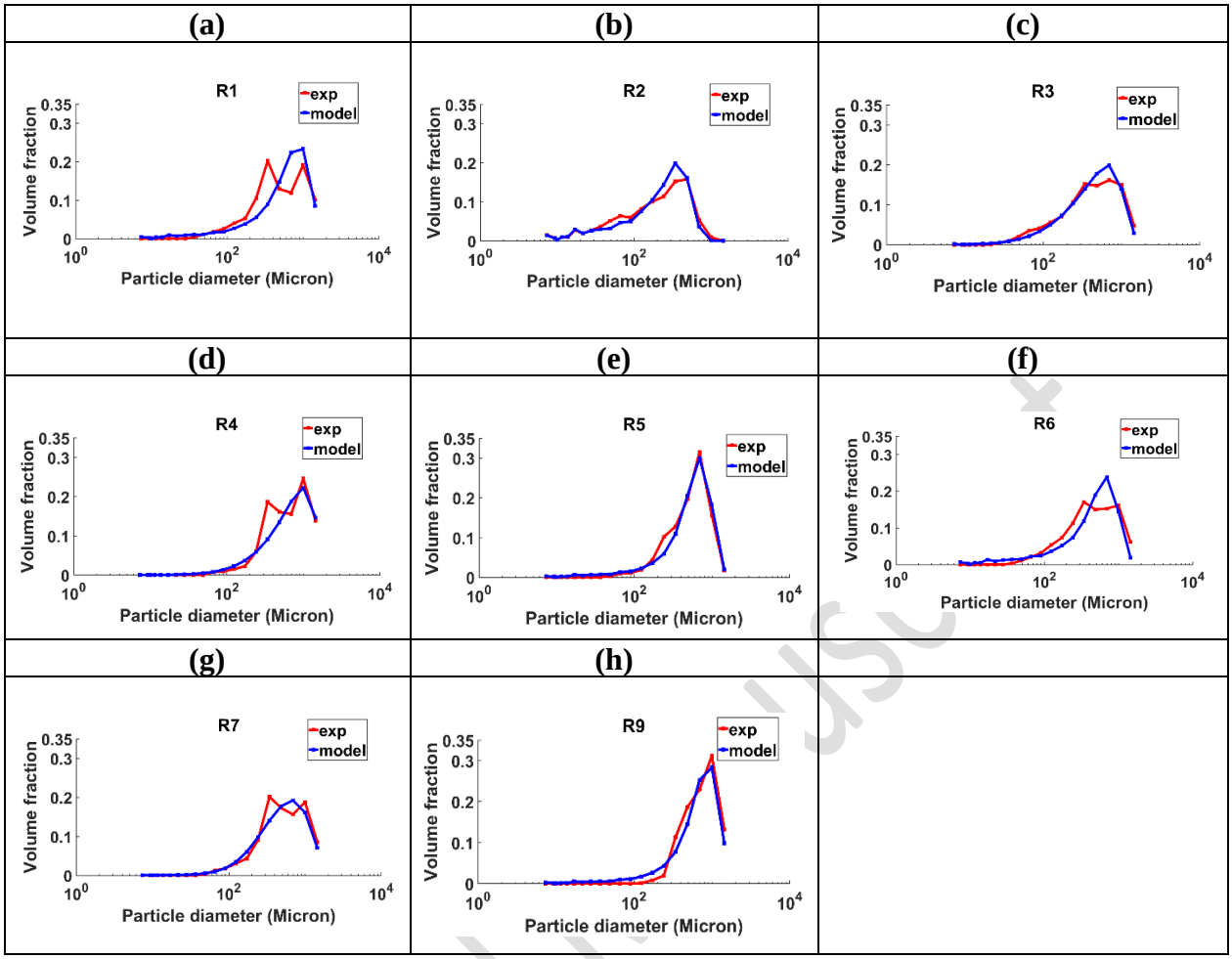

Figure 8: Experimental vs. predicted PSDs for calibrating the empirical parameters using sum kernel with FVNM.

Figures 7 and 8 provide the comparison of experimental and predicted PSDs for Kapur's and sum kernels, respectively. The results reveal that Kapur's kernel shows better fitting than sum kernel corresponding to various L/S ratios and screw speeds. Also it shown that the 1-D PBM prediction has difficulty in capturing bimodality distributions very accurately, since the liquid particle distribution plays also a role in the aggregation and breakage mechanisms. Still Kapur's kernel provided a better accuracy compared to sum kernel. For tracking bimodality behaviour more accurately higher dimensional PBM is required to account for liquid distribution.

7.3. Effect of numerical solution

Choosing the appropriate numerical method to solve the CPBM is very important in predicting the numerical solutions with high accuracy. The effect of the mass conservation property corresponding to different numerical methods is discussed in detail in this section. FVNM and CANM are used to solve the CPBM using the Kapur's kernel. For the comparison, 20 particle size bins are considered for both methods.

Figure 9 shows the comparison of the experimental and predicted PSDs for Kapur's using the CANM. It is observed that PSDs predicted by the CANM show large deviation from the experimental results for each run, whereas the FVNM performs much better than the CANM as shown in Figure 7 where it show less deviation from the experimental results. The effect of deviation can also be seen in the mass conservation property which can be calculated by $\sum_{i=1}^{p} u_i N_i$. Table 4 shows that more mass is lost from the system when the CPBM is solved using the CANM whereas less mass is lost from the system when the CPBM is approximated using the FVNM. This is due to the fact that the CANM is based on the distribution of the particles to the neighbouring nodes when the average of the particle's properties is not matched with the representative to ensure the conservation of the required properties. However, in case of the FVNM, no distribution of the particles is required as the conservation of the required properties are achieved by introducing the weight functions. Table 3 shows that the CANM has a mass loss range between 2.5 – 25 % with an average of 14 %, while FVNM has a mass loss range between 0- 3% with an average of 1.5%. The values for the empirical parameters of aggregation and breakage kernels in the conveying and kneading zones are given in Appendix D.

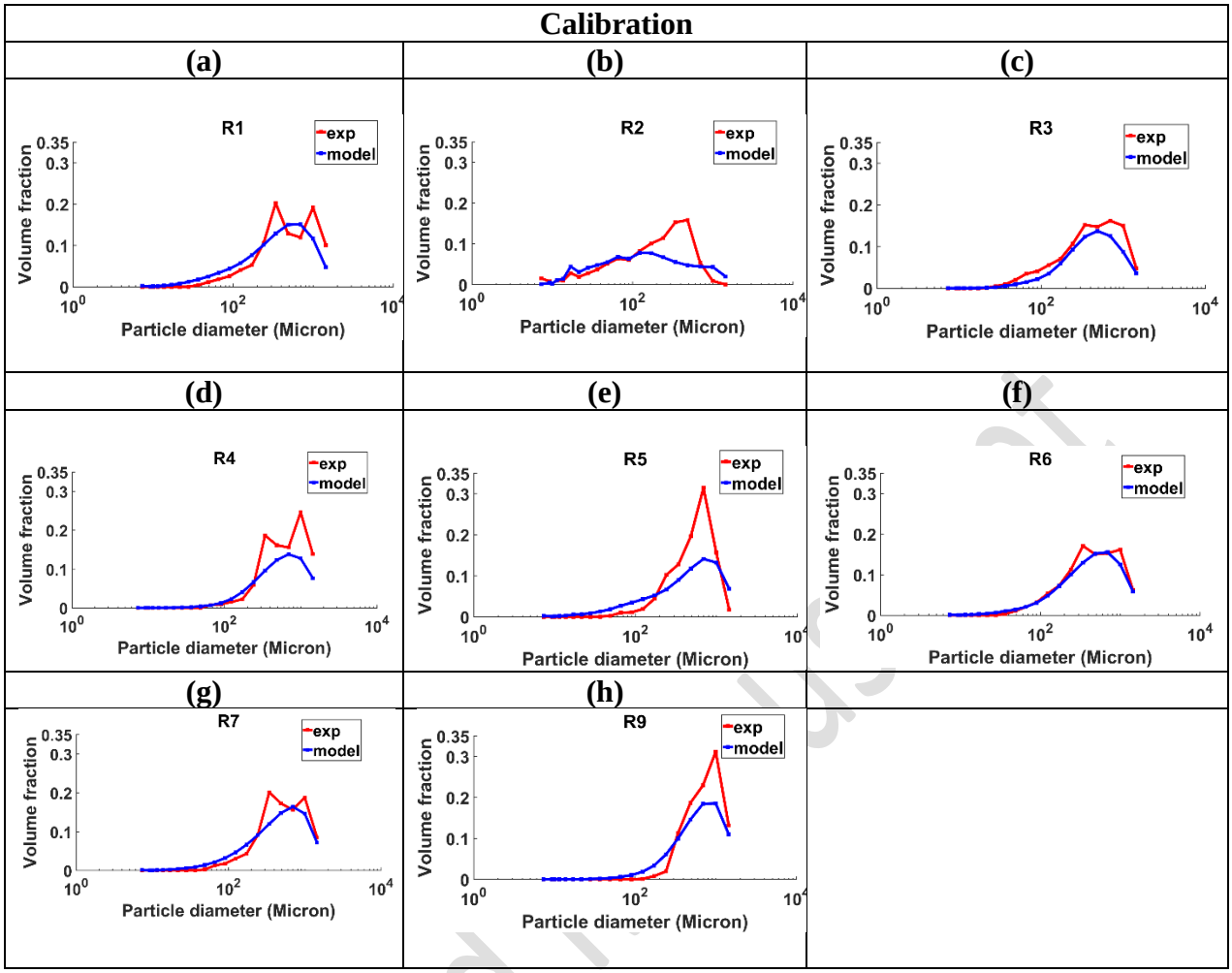

Figure 9: Experimental vs. predicted PSDs using Kapur's kernel using CANM.

Table 4: First moment ($\sum_{i=1}^{p} u_i N_i$) for FVNM and CANM respectively.

Run	FVNM	CANM
1	0.9832	0.9776
2	1	0.8094
3	0.9889	0.7507
4	0.9751	0.963
5	0.9999	0.8274
6	0.9976	0.9306
7	0.9846	0.9453
9	0.9927	0.8599

7.4. Deriving and validating the CPBM

7.4.1. Calibration and fitting

Kapur and linear power selection kernels are used as aggregation and breakage kernels, respectively and FVNM is used for solving the CPBM. In calibrating the PBM, ten empirical constants in the aggregation and breakage kernels are calibrated using GA optimization in Matlab with 8 of the 9 experimental runs of the DOE. The obtained values of the empirical parameters are provided in Table 5.

The obtained values show that the aggregation rate $\frac{\beta_0(u_i+u_j)^a}{(u_i u_j)^b}$ in the conveying zone is higher than for the kneading zone in runs 1 to 6 where L/S ratio is 0.9 and 1.1, while the aggregation rate is lower for runs 7 and 9 where the L/S ratio is 1.3. This shows that there is more aggregation in the conveying zone at low and medium liquid content while more aggregation in the kneading zone at higher liquid content. At low and medium liquid content in the kneading zone, the high shearing will keep preventing the particles from aggregating and prone to more breakage. While at high liquid content, high shearing in the kneading zone will better mix the powder and liquid than the conveying zone, which in turn improve the aggregation rates.

Moreover, high shearing in kneading zones will cause the breakage rate $S_0 u_i^k$ to be higher in the kneading zones than the conveying zones for all runs (See Table 5).

Table 5: Empirical parameters after calibration for eight experimental runs

Empirical parameters	**Runs**							
	1	**2**	**3**	**4**	**5**	**6**	**7**	**9**
β_0(CZ)	40.708	99.764	68.376	35.967	39.09	28.432	85.212	33.483
a(CZ)	3.947	2.254	2.434	3.394	3.813	1.97	3.986	7.419
b(CZ)	1.078	0.4	0.354	0.947	0.926	0.317	1.173	1.908
S_0(CZ)	77.213	53.091	55.008	14.602	60.455	66.028	3.029	99.892

k(CZ)	1.097	2.506	0.364	0.204	2.537	2.405	0.149	1.908
β_0(KZ)	26.533	99.771	40.965	33.363	26.062	29.207	63.665	33.398
a(KZ)	2.413	1.325	5.054	5.541	1.352	2.903	5.682	3.941
b(KZ)	0.543	0	1.677	1.809	0.066	0.567	1.949	1.207
S_0(KZ)	11.643	41.834	10.588	99.004	22.655	36.091	56.128	24.517
k(KZ)	0.104	2.5	0.045	0.256	0.23	0.198	0.254	0.252

Since the empirical constants are changing for each run with different process parameters (L/S ratio and screw speed) and thus giving a different PSD, an equation can be obtained to represent the empirical parameters in terms of the process parameters in such a way that each empirical parameter is replaced by an equation in terms of L/S ratio and screw speed. Since the number of experimental points of the empirical parameters are not enough to fit an accurate model for the empirical parameters, Kriging interpolation is used to interpolate for empirical parameters data points at new process parameters (L/S ratio and screw speed) using additional 36 experimental points (refer to Appendix B). The kriging interpolation was cross-validated for all the 8 experimental data points used, where cross-validation omits a data point and then interpolates this value using the remaining data points, the interpolated and actual values are then compared and if the error is high a new variogram is optimized. Also, to account for the nonlinearity of the relations with the optimum number of constants in the equations, fifth order polynomial equations are used as the functions which can best fit the empirical parameters from the kriging model in terms of the process parameters.

The 36 interpolated points were split with 30 being used to fit the polynomial curve to the data points with a 95% confidence interval and 6 being used for validating the fitting.

The general form of the fitted polynomial equations of the empirical parameters in terms of the process parameters is given in equation (31), where $f(SS, L/S)$ represents the empirical parameters of the aggregation and breakage kernels in terms of L/S ratio and screw speed (SS)

and p_{ij}s are the polynomial constants. The values of p_{ij}s are given in Table 6 after fitting the polynomial equations with the 95% confidence interval of p_{ij}s given in Appendix E.

$$f(SS, L/S) = p_{00} + p_{10} * SS + p_{01} * \frac{L}{S} + p_{20} * SS^2 + p_{11} * SS * \frac{L}{S} + p_{02} * \left(\frac{L}{S}\right)^2 + p_{30} * SS^3 + p_{21} * SS^2 * \frac{L}{S} + p_{12} * SS * \left(\frac{L}{S}\right)^2 + p_{03} * \left(\frac{L}{S}\right)^3 + p_{40} * SS^4 + p_{31} * SS^3 * \frac{L}{S} + p_{22} * SS^2 * \left(\frac{L}{S}\right)^2 + p_{13} * SS * \left(\frac{L}{S}\right)^3 + p_{04} * \left(\frac{L}{S}\right)^4 + p_{50} * SS^5 + p_{41} * SS^4 * \frac{L}{S} + p_{32} * SS^3 * \left(\frac{L}{S}\right)^2 + p_{23} * SS^2 * \left(\frac{L}{S}\right)^3 + p_{14} * SS * \left(\frac{L}{S}\right)^4 + p_{05} * \left(\frac{L}{S}\right)^5 \quad (31)$$

where $f(SS, L/S)$ is the fitted empirical parameters.

Table 6: Fitting and validation of the polynomial model fitted for the empirical parameters in the CZ and KZ.

	Training			Validation	
empirical parameters	**SSE**	**R2**	**RMSE**	**SSE**	**RMSE**
β_0(CE)	120.0327	0.964	3.4645	533.35	10.3281
a(CE)	0.11156	0.998	0.1056	0.0810	0.12730
b(CE)	0.00680	0.999	0.0260	0.0080	0.04006
S_0(CE)	67.0594	0.995	2.5895	26.108	2.28508
K(CE)	0.30726	0.941	0.1752	0.1286	0.16037
β_0(KZ)	97.7606	0.958	3.1266	713.719	11.9475
a(KZ)	0.13208	0.998	0.1149	0.02917	0.07638
b(KZ)	0.015836	0.998	0.0398	0.00471	0.03069
S_0(KZ)	134.7831	0.954	3.6712	34.167	2.61410
K(KZ)	0.12826	0.979	0.1133	0.7527	0.38800

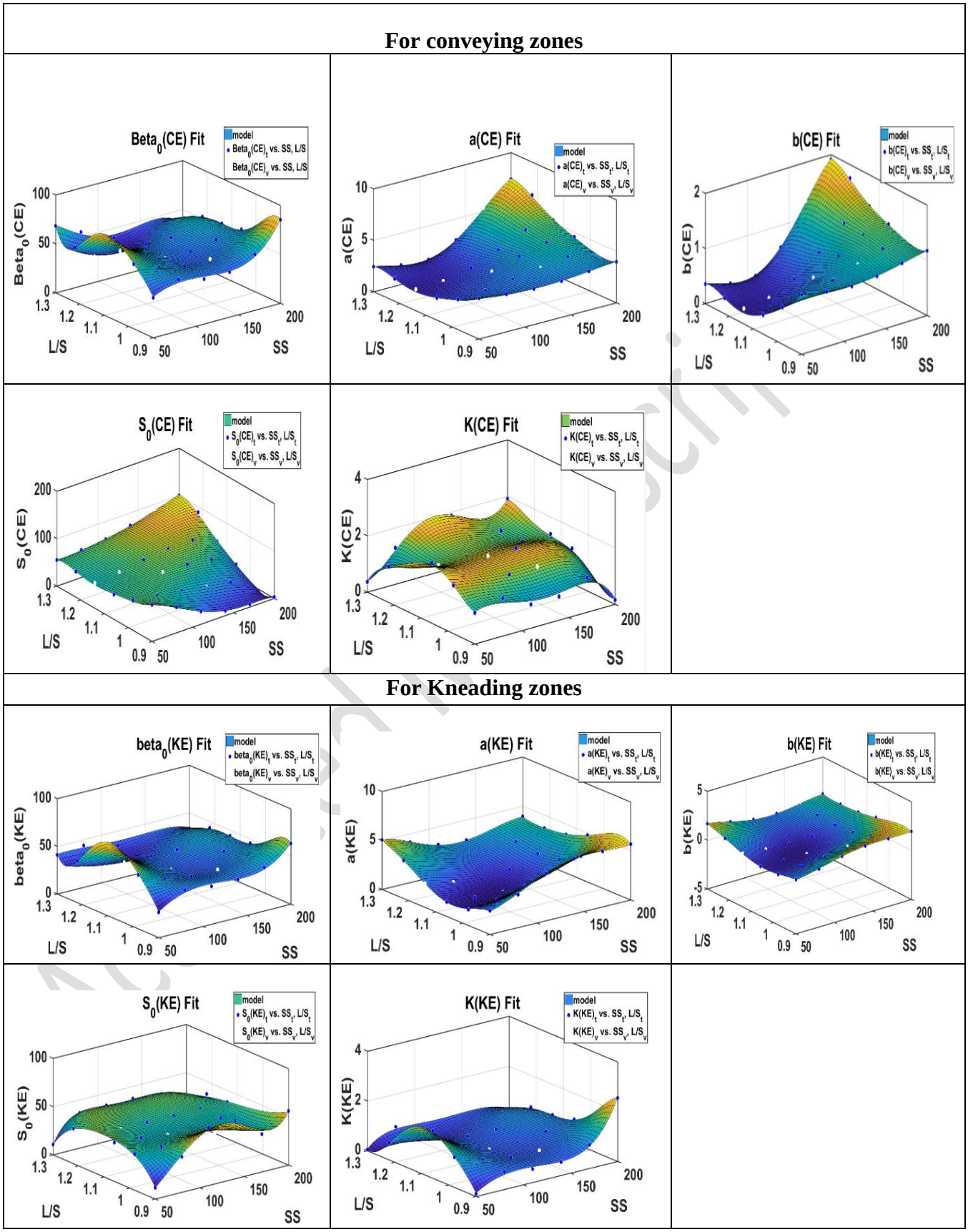

Figure 10: Fitting the empirical parameters to the process parameters in a polynomial equation for the conveying and kneading elements.

Table 7: Values of polynomial equations constants after fitting the empirical parameters in terms of L/S and screw speed.

Const.	β_0(CE)	a(CE)	b(CE)	S0(CE)	KCE	β_0(KZ)	a(KZ)	b(KZ)	S0(KZ)	K(KZ)
p_{00}	49.32	3.505	0.7971	64.59	1.632	39.56	1.329	-0.0049	34.75	0.5973
p_{10}	0.4855	1.567	0.5233	3.017	0.04509	1.525	0.8548	0.3991	2.553	0.08525
p_{01}	4.684	-0.7673	-0.3054	12.45	-0.4046	5.036	-0.04902	-0.1464	2.082	0.1316
p_{20}	11.26	0.3118	0.09546	-6.057	-0.06551	10.29	0.9073	0.407	-0.3324	0.3754
p_{11}	11.06	0.8924	0.2488	21.8	-0.06866	8.009	-1.123	-0.464	3.015	0.3044
p_{02}	-6.143	-0.2248	-0.01496	-12.55	-0.3822	-3.738	2.266	0.9166	11.96	-0.09758
p_{30}	-4.846	-0.2291	-0.06388	-2.258	-0.04662	-5.641	-0.03474	-0.0193	-5.017	-0.272
p_{21}	-0.6738	0.7966	0.211	0.8699	-0.3118	-1.464	0.4956	0.2599	9.997	0.03241
p_{12}	13.69	-0.286	-0.1153	-5.308	-0.1227	10.57	-0.1738	-0.1067	-5.292	0.2464
p_{03}	-15.97	0.675	0.1769	14.23	0.8428	-15	-0.924	-0.3012	-5.637	-0.3908
p_{40}	-1.128	-0.1797	-0.04549	-2.366	0.02132	-0.3637	-0.03261	-0.0169	1.792	-0.01352
p_{31}	-6.099	-0.05665	-0.01613	-0.6408	0.1762	-4.097	0.02089	0.01035	-2.869	-0.1976
p_{22}	-1.507	0.4319	0.1116	10.28	-0.1076	-4.515	-0.4408	-0.1645	-7.173	-0.108
p_{13}	-3.709	-0.07375	-0.01502	-2.827	-0.00327	-2.36	0.2888	0.1137	-1.098	-0.1016
p_{04}	1.453	-0.02934	-0.0148	0.6654	0.1476	1.56	-0.4154	-0.1568	-2.136	0.02608
p_{50}	0.01082	-0.02909	-0.00546	-1.107	-0.04509	-0.2259	0.04289	0.02046	1.653	0.03141
p_{41}	-1.673	-0.1265	-0.0344	1.201	0.2258	-1.004	-0.218	-0.09554	-5.724	-0.09882
p_{32}	3.199	0.09412	0.01995	2.674	0.1061	5.01	-0.06975	-0.03135	3.759	0.241
p_{23}	1.285	-0.1024	-0.02583	-3.5	-0.12	1.452	0.2561	0.09649	2.067	-0.01027
p_{14}	-6.924	0.02248	0.01632	0.2417	0.03144	-6.16	-0.00075	0.01092	1.514	-0.1596
p_{05}	6.507	-0.2456	-0.06143	-5.288	-0.2285	6.011	0.2339	0.07321	0.06777	0.1612

Table 6 shows the goodness of the fit based on SSE, R^2 and root mean squared error (RMSE) in the training and validation phases, respectively. The fitted fifth order polynomial equations show a very good fit with R^2 whose values lies between 0.941 and 0.998 with an average of 0.990 in the training phase. Also, the validation of the model shows a very good RMSE between 1- 5% of the mean. Figure 10 shows graphically the polynomial fitting where some of the curves show a high nonlinear relationship between the empirical parameters and the process parameters and Table 7 gives the values of the polynomial constants with 95% confidence. The points used for training are the blue dots and the ones used for validation are the white dots. After validating the model, the polynomial equations are substituted for the empirical parameters in the aggregation and breakage kernels of the CPBM.

7.4.2. Model validation

By replacing the empirical parameters in the aggregation and breakage kernels with the polynomial functions obtained, the CPBM can now predict the PSD based only on the process parameters: L/S ratio and screw speed of the twin screw.

To validate the accuracy of the developed CPBM, the experimental PSD obtained from runs 8, 10 and 11 are used to compare with the predicted PSD from the CPBM in terms of L/S ratio and screw speed. Runs 8, 10 and 11 are conducted using MCC-101 at L/S ratio of 1.3, 1.15 and 1.05 respectively and screw speeds 100, 150 and 170 rpm respectively. These values are replaced in the developed model and the predicted versus the experimental PSDs for runs 8, 10 and 11 are shown in Figures 11, 12 and 13 respectively. The model gives a very good prediction for runs 8, 10 and 11 with R^2 = 0.895, 0.9578, and 0.886 respectively and SSE = 0.0282, 0.0083 and 0.0148 respectively and mass conservation ($\sum_{i=1}^{p} \boldsymbol{u_i N_i}$) 0.9995, 0.9999 and 0.9991 respectively.

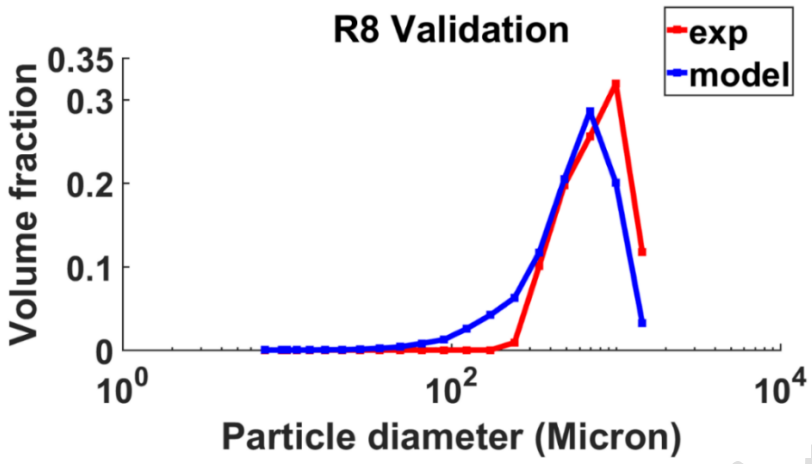

Figure 11: Experimental vs. predicted PSD for run 8.

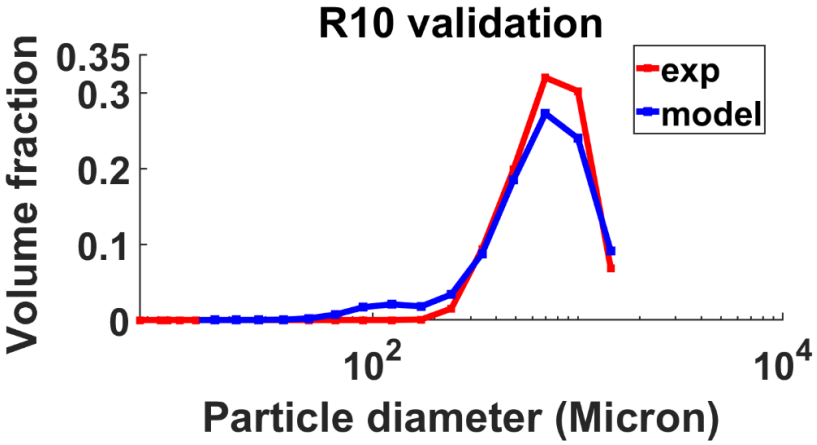

Figure 12: Experimental vs. predicted PSD for run 10.

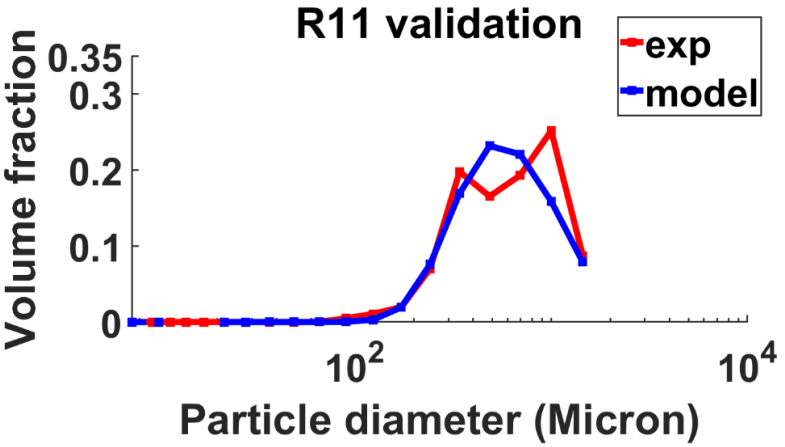

Figure 13: Experimental vs. predicted PSD for run 11.

The developed CPBM model will be used in further work as a simulation plant (predictive model) to derive a state space for a model predictive controller (MPC). The MPC can be applied to control the PSD in TSG by the L/S ratio and screw speed.

8. Conclusion

Continuous wet granulation in twin screw has been modelled using CPBM. The predictive CPBM calculates the PSD based on twin screw process parameters (L/S ratio and screw speed (rpm)) and has been calibrated and validated from experimental PSD obtained at various L/S ratios and screw speeds. The current model accounts for the spatial inhomogeneity of the screw configurations by representing them in terms of different aggregation and breakage kernels. Results show that aggregation is higher in the conveying zones than kneading zones at low and medium L/S ratio while breakage is higher in the kneading zones for all L/S ratios and screw speeds. It has been also shown that Kapur's kernel provides better flexibility compared to the sum kernel. Moreover, the finite volume numerical method showed a better accuracy in solving the CPBM compared to cell average.

Appendix A

Cell Average Numerical Method (CANM)

The mathematical formulation of the cell average numerical method can be derived by substituting equation (14) in equation (8) and integrating over each cell, the following set of ODE's are formed which is given by

$$\frac{dN_i}{dt} = B_i - D_i,$$

where the birth term for CANM given by

$$B_i = \sum_{u_{i-\frac{1}{2}} \le (u_j+u_k) < u_{i+\frac{1}{2}}}^{j \le k} \left(1 - \frac{1}{2}\delta_{j,k}\right) \beta(u_j, u_k) N_j N_k + \sum_{k \ge i} N_k S_k \int_{u_{-\frac{1}{2}}}^{p_k^i} b(u, u\_uk) du \quad (32)$$

and the death term by

$$D_i = \sum_{j=1}^{I} \beta\left(u_i, u_j\right) N_i N_j + S_i\, N_i. \tag{33}$$

The CANM is based upon the concept of averaging all properties of the particles in a cell and distributing the property between the two nodes that bracket the cell. Accordingly, the mass of new particles that are formed inside the *i*th cell is re-distribute between nodes i and $i+1$ by the respective factors a and b whose values are determined such that the zeroth and first moments of the population are strictly conserved. These factors are obtained by solving

$$a u_i + b u_{i+1} = B_i \bar{u}_i \quad a + b = B_i. \tag{34}$$

Here, $\bar{u}_i$ is the mean size of new particles that ow by aggregation in the *i*th cell,

$$\bar{u}_i = \frac{V_i}{B_i}, \tag{35}$$

and V_i is the flux of particle mass into the cell,

$$V_i = \sum_{u_{i-1/2} \le (u_j + u_k) < u_{i+1/2}}^{j \le k} (1 - \frac{1}{2}\delta_{j,k})\ \beta\left(u_j, u_k\right) N_j N_k \left(u_j + u_k\right) +$$

$$\sum_{k \ge i} N_k S_k \int_{u_{-\frac{1}{2}}}^{p_k^i} ub(u, u\_uk) du \tag{36}$$

Solving the system of equations (7), we get

$$a = b_i \lambda_i^+(\bar{u}_i), \quad b = b_i \lambda_{i+1}^-(\bar{u}_i), \tag{37}$$

where the functions λ_i^+ and λ_i^- are given by

$$\lambda_i^{\pm} = (u - u_{i\pm1})/(u_i - u_{i\pm1}). \tag{38}$$

In summary, after collecting all contributions to the birth at u_i and the modified birth takes the following form

$$B_i^{mod} = B_{i-1}\lambda_i^-(\bar{u}_{i-1}) H(\bar{u}_{i-1} - x_{i-1}) + B_i \lambda_i^-(\bar{u}_i) H(x_i - \bar{u}_i) +$$

$$B_i \lambda_i^+(\bar{u}_i)\, H(\bar{u}_i - x_i) + B_{i+1}\lambda_{i+1}^+(\bar{u}_{i+1}) H(x_{i+1} - \bar{u}_{i+1}) \tag{39}$$

Putting the above expression in equation (4), the final set of ODE's formed are

$$\frac{dN_i}{dt} = \ B_{i-1}\lambda_i^-(\bar{u}_{i-1}) H(\bar{u}_{i-1} - x_{i-1}) + B_i \lambda_i^-(\bar{u}_i) H(x_i - \bar{u}_i) + \ B_i \lambda_i^+(\bar{u}_i) H(\bar{u}_i - x_i) +$$

$$B_{i+1}\lambda_{i+1}^+(\bar{u}_{i+1}) H(x_{i+1} - \bar{u}_{i+1}) - \sum_{j=1}^{I} \beta\left(u_i, u_j\right) N_i N_j. \tag{40}$$

where the Heaviside step function is defined by

$$H(u-u_i)=\begin{cases}1,\ u-u_i>0\\ \frac{1}{2},\ u-u_i=0\\ 0,\ u-u_i<0.\end{cases} \quad (41)$$

The detailed formulation of the cell average technique can be found in Kumar et al.

(2006)[24].

Appendix B

Empirical parameters interpolations after kriging interpolation given in supplementary excel sheet 1.

Appendix C

Values of the empirical parameters after calibration using sum and Kapur kernels given in supplementary excel sheet 2.

Appendix D

Values of the empirical parameters after calibration using FVNM and CANM given in supplementary excel sheet 3.

Appendix E

Interval of confidence for the polynomial constants obtained after fitting the polynomial equations are given in supplementary excel sheet 4.

Appendix F

Kriging interpolation is based on the nearest neighbourhood method, where it predicts a response y_k at an interpolated point x_k using the weighted sum of the known responses (y_1, y_2, …, y_n) in which x_k falls in the neighbourhood of their corresponding sampling points (x_1, x_2, x_3…, x_n) [35], where:

$$y_k = f(x_k) = \sum_{i=1}^{p} w_i f(x_i) \quad (25)$$

w_i is the weighted sum (kriging weights) that depends on the Euclidian distance h where

$$h = \|x_i - x_j\| \quad (26)$$

Kriging algorithm determines the kriging weights for each group of p clustered points in the neighbourhood of x_k, where the obtained variogram model forces the sum of the kriging weights to unity. In calculating $f(x_k)$, $f(x_i)'s$ corresponding to $x_i's$ in the neighbourhood of x_k and nearer to x_k will have more weight towards determining $f(x_k)$. Also, with the higher number of neighbouring points and the nearer they are to x_k, the better $f(x_k)$ can be predicted with more confidence.

The kriging variogram is derived from the data point observations to statistically quantify the dataset roughness that complements histograms and other descriptive statistics (exponential, Gaussian, cubic, etc.). The variogram depends on the Euclidian distance h, at each variance difference of the observations in the neighbourhood of x_k, where:

$$\gamma(h) = \frac{1}{2}[var(y_i - y_j)] \tag{27}$$

After fitting the derived variogram to a variogram model the covariance at each *h* is calculated by:

$$Cov(h) = \sigma^2_{max} - \gamma(h) \tag{28}$$

σ^2_{max} is the maximum variance of the variogram function. The covariance is then used to calculate the kriging weight at each point by solving the following system:

$$\begin{bmatrix} Cov(d_{1,1}) & \dots & Cov(d_{1,N}) & 1 \\ \vdots & \ddots & \vdots & \vdots \\ Cov(d_{N,1}) & \dots & Cov(d_{N,N}) & 1 \\ 1 & \dots & 1 & 0 \end{bmatrix} \times \begin{bmatrix} w_1 \\ \vdots \\ w_N \\ \lambda \end{bmatrix} = \begin{bmatrix} Cov(d_{1,k}) \\ \vdots \\ Cov(d_{N,k}) \\ 1 \end{bmatrix} \tag{29}$$

where $Cov(d_{i,j})$ and $Cov(d_{i,k})$ are the covariances of the distance $d_{i,j}$ and $d_{i,k}$ between sampling points x_i - x_j and x_i - x_k (interpolated point). At each interpolated point x_k the variance is calculated by equation 30.

$$\sigma_k^2 = \sigma_{max}^2 - \sum_{i=1}^{N} w_i Cov(d_{i,k}) - \lambda \quad (30)$$

Symbols and Abbreviations

Symbols

agg	aggregation
β	aggregation rate
B	birth rate of particles
br	breakage
S	breakage rate
i	bin number
I	boundary of each bin
p	constant
D	death rate of particles
h	Euclidian distance
β_0	empirical parameter
a	empirical parameter
b	empirical parameter
S_0	empirical parameter
k	empirical parameter
X	empirical parameters dummy variable
y_k	interpolated point
w_i	kriging weight
σ_{max}^2	maximum variance
y_i	measured volume density at size bin i
λ	mean residence time (seconds)
N	number of particles
OF	objective function

1-D	one dimension
v , ϵ and u	particle volume
b	probability density function
ϕ	powder flow rate (g/s)
$f_i(X)$	predicted volume density at size bin i
n	represents density of particles population
t	time
u_{max}	upper volume limit of particle size
$\omega_{j,k}^b, \omega_{j,k}^d, \theta_k^b$ and θ_k^d	weight factors

Abbreviations

APIs	active pharmaceutical ingredients
ANN	artificial neuron network
CPBM	compartmental population balance model
CANM	cell average numerical method
CZ	conveying zone
CA	cell average
CE	conveying elements
Cov	covariance
DOE	design of experiment
DEM	discrete elemental modelling
FVNM	finite volume numerical method
GA	Generic Algorithm
KZ	kneading zone
KE	kneading elements
L/S	liquid to solid ratio
MPC	model predictive controller
MCC-101	microcrystalline cellulose -101

ODEs	ordinary differential equations
PBM	population balance model
PSD	particle size distribution
QbD	Quality-by-Design
RMSE	root mean squared error
R^2	root squared error
SSE	sum of squared error
SS	screw speed (rpm)
TSG	twin screw granulator

Acknowledgment

This work was funded by Enterprise Ireland (EI).

This work was funded by Science Foundation Ireland (SFI) under the following grants:

Model Predictive Control of Continuous Pharmaceutical Processes - (13/IA/1980).

The equipment used in this work was funded by Science Foundation Ireland (SFI) under the following grants:

Model Predictive Control of Continuous Pharmaceutical Processes - (13/IA/1980).

This research was made possible with the support of Pharmaceutical Manufacturing Technology Centre (PMTC) as well as Synthesis and Solid State Pharmaceutical Centre (SSPC).

The authors gratefully acknowledge the financial support provided by Marie Skłodowska-Curie Individual Fellowship no. 841906 to Dr. Mehakpreet Singh.

References

[1] S. L. Lee *et al.*, "Modernizing Pharmaceutical Manufacturing: from Batch to Continuous Production," *J. Pharm. Innov.*, vol. 10, no. 3, pp. 191–199, 2015.

[2] S. Mascia *et al.*, "End-to-end continuous manufacturing of pharmaceuticals: Integrated synthesis, purification, and final dosage formation," *Angew. Chemie - Int. Ed.*, vol. 52, no. 47, pp. 12359–12363, 2013.

[3] M. Sakai, Y. Shigeto, G. Basinskas, A. Hosokawa, and M. Fuji, "Discrete element simulation for the evaluation of solid mixing in an industrial blender," *Chem. Eng. J.*, vol. 279, pp. 821–839, 2015.

[4] P. Suresh, I. Sreedhar, R. Vaidhiswaran, and A. Venugopal, "A comprehensive review on process and engineering aspects of pharmaceutical wet granulation," *Chemical Engineering Journal*, vol. 328. pp. 785–815, 2017.

[5] T. C. Seem *et al.*, "Twin screw granulation - A literature review," *Powder Technol.*, vol. 276, pp. 89–102, 2015.

[6] R. M. Dhenge, R. S. Fyles, J. J. Cartwright, D. G. Doughty, and M. J. Hounslow, "Twin screw wet granulation: Granule properties," *Chem. Eng. J.*, vol. 164, no. 2–3, pp. 322–329, Nov. 2010.

[7] A. S. Patil and A. M. Pethe, "Quality by design (QbD): A new concept for development of quality pharmaceuticals," *Int. J. Pharm. Qual. Assur.*, vol. 4, no. 2, pp. 13–19, 2013.

[8] A. Kumar, K. V. Gernaey, T. De Beer, and I. Nopens, "Model-based analysis of high shear wet granulation from batch to continuous processes in pharmaceutical production - A critical review," *Eur. J. Pharm. Biopharm.*, vol. 85, no. 3 PART B, pp. 814–832, 2013.

[9] J. Litster and B. Ennis, *The Science and Engineering of Granulation Processes*, vol. 15, no. 1. Dordrecht: Springer Netherlands, 2004.

[10] A. Chaudhury, H. Wu, M. Khan, and R. Ramachandran, "A mechanistic population balance model for granulation processes: Effect of process and formulation parameters," *Chem. Eng. Sci.*, vol. 107, pp. 76–92, 2014.

[11] G. Kaur, M. Singh, J. Kumar, T. De Beer, and I. Nopens, "Mathematical Modelling and Simulation of a Spray Fluidized Bed Granulator," *Processes*, vol. 6, no. 10, p. 195, 2018.

[12] Y. K. Ho, C. Kirse, H. Briesen, M. Singh, C. H. Chan, and K. W. Kow, "Towards improved predictions for the enzymatic chain-end scission of natural polymers by population balances: The need for a non-classical rate kernel," *Chem. Eng. Sci.*, vol. 176, pp. 329–342, 2018.

[13] S. Shirazian, H. Y. Ismail, M. Singh, R. Shaikh, D. M. Croker, and G. M. Walker, "Multi-dimensional population balance modelling of pharmaceutical formulations for

continuous twin-screw wet granulation : Determination of liquid distribution," *Int. J. Pharm.*, vol. 566, no. January, pp. 352–360, 2019.

[14] M. Singh, H. Y. Ismail, R. Singh, A. B. Albadarin, and G. Walker, "Finite volume approximation of nonlinear agglomeration population balance equation on triangular grid," *J. Aerosol Sci.*, vol. 137, no. May, p. 105430, 2019.

[15] D. Barrasso, A. Tamrakar, and R. Ramachandran, "Model order reduction of a multi-scale PBM-DEM description of a wet granulation process via ANN," *Procedia Eng.*, vol. 102, pp. 1295–1304, 2015.

[16] D. Barrasso and R. Ramachandran, "Multi-scale modeling of granulation processes: Bi-directional coupling of PBM with DEM via collision frequencies," *Chem. Eng. Res. Des.*, vol. 93, pp. 304–317, 2015.

[17] D. Van Hauwermeiren *et al.*, "On the modelling of granule size distributions in twin-screw wet granulation: Calibration of a novel compartmental population balance model," *Powder Technol.*, 2018.

[18] A. Darelius, A. Rasmuson, I. N. Björn, and S. Folestad, "High shear wet granulation modelling - A mechanistic approach using population balances," *Powder Technol.*, vol. 160, no. 3, pp. 209–218, 2005.

[19] T. Glaser *et al.*, "Model predictive control of continuous drum granulation," *J. Process Control*, vol. 19, no. 4, pp. 615–622, 2009.

[20] F. Y. Wang, X. Y. Ge, N. Balliu, and I. T. Cameron, "Optimal control and operation of drum granulation processes," *Chem. Eng. Sci.*, vol. 61, no. 1, pp. 257–267, 2006.

[21] H. Liu *et al.*, "Development of a three-compartmental population balance model for a continuous twin screw wet granulation process," *Pharm. Dev. Technol.*, vol. 0, no. 0, pp. 1–39, 2018.

[22] M. J. Hounslow, R. L. Ryall, and V. R. Marshall, "A discretized population balance for nucleation, growth, and aggregation," *AIChE J.*, vol. 34, no. 11, pp. 1821–1832, Nov. 1988.

[23] S. Kumar and D. Ramkrishna, "On the solution of population balance equations by discretization—I. A fixed pivot technique," *Chem. Eng. Sci.*, vol. 51, no. 8, pp. 1311–1332, Apr. 1996.

[24] J. Kumar, "Numerical approximations of population balance equations in particulate systems," *Cell*, p. 239, 2006.

[25] J. Saha, J. Kumar, A. Bück, and E. Tsotsas, "Finite volume approximations of breakage population balance equation," *Chem. Eng. Res. Des.*, vol. 110, pp. 114–122, 2016.

[26] E. Tsotsas, G. Kaur, and J. Kumar, "An accurate and efficient discrete formulation of aggregation population balance equation," *Kinet. Relat. Model.*, vol. 9, no. 2, pp. 373–391, 2016.

[27] M. Singh, J. Kumar, A. Bück, and E. Tsotsas, "A volume-consistent discrete formulation of aggregation population balance equations," *Math. Methods Appl. Sci.*,

vol. 39, no. 9, pp. 2275–2286, 2016.

[28] P. C. Kapur, “Kinetics of granulation by non-random coalescence mechanism,” *Chem. Eng. Sci.*, vol. 27, no. 10, pp. 1863–1869, 1972.

[29] R. M. Dhenge, R. S. Fyles, J. J. Cartwright, D. G. Doughty, M. J. Hounslow, and A. D. Salman, “Twin screw wet granulation: Granule properties,” *Chem. Eng. J.*, vol. 164, no. 2–3, pp. 322–329, 2010.

[30] W. Meng, S. Oka, X. Liu, T. Omer, R. Ramachandran, and F. J. Muzzio, “Effects of Process and Design Parameters on Granule Size Distribution in a Continuous High Shear Granulation Process,” *J. Pharm. Innov.*, vol. 12, no. 4, pp. 283–295, 2017.

[31] A. Rogers, A. Hashemi, and M. Ierapetritou, “Modeling of Particulate Processes for the Continuous Manufacture of Solid-Based Pharmaceutical Dosage Forms,” *Processes*, vol. 1, no. 2, pp. 67–127, 2013.

[32] D. Ramkrishna, *Population balances*, vol. 1. 2000.

[33] A. Kumar *et al.*, “European Journal of Pharmaceutics and Biopharmaceutics Mixing and transport during pharmaceutical twin-screw wet granulation : Experimental analysis via chemical imaging,” *Eur. J. Pharm. Biopharm.*, vol. 87, no. 2, pp. 279–289, 2014.

[34] H. Y. Ismail *et al.*, “Developing ANN-Kriging hybrid model based on process parameters for prediction of mean residence time distribution in twin-screw wet granulation,” vol. 343, pp. 568–577, 2019.

[35] J. Kumar, G. Warnecke, M. Peglow, and S. Heinrich, “Comparison of numerical methods for solving population balance equations incorporating aggregation and breakage,” *Powder Technol.*, vol. 189, no. 2, pp. 218–229, 2009.